Correspondence and
requests for materials
should be addressed to
Y.-R.M. (ronma@mail.
ndhu.edu.tw)

Photoluminescence mechanisms of metallic Zn nanospheres, semiconducting ZnO nanoballoons, and metal-semiconductor Zn/ZnO nanospheres

Jin-Han Lin[1,2], Ranjit A. Patil[1], Rupesh S. Devan[1], Zhe-An Liu[1], Yi-Ping Wang[3], Ching-Hwa Ho[3], Yung Liou[2] & Yuan-Ron Ma[1]

[1]Department of Physics, National Dong Hwa University, Hualien 97401, Taiwan, R.O.C, [2]Institute of Physics, Academia Sinica, Taipei 11529, Taiwan, R.O.C, [3]Graduate Institute of Applied Science and Technology, National Taiwan University of Science and Technology, Taipei 106, Taiwan, R.O.C.

We utilized a thermal radiation method to synthesize semiconducting hollow ZnO nanoballoons and metal-semiconductor concentric solid Zn/ZnO nanospheres from metallic solid Zn nanospheres. The chemical properties, crystalline structures, and photoluminescence mechanisms for the metallic solid Zn nanospheres, semiconducting hollow ZnO nanoballoons, and metal-semiconductor concentric solid Zn/ZnO nanospheres are presented. The PL emissions of the metallic Zn solid nanospheres are mainly dependent on the electron transitions between the Fermi level (E_F) and the 3d band, while those of the semiconducting hollow ZnO nanoballoons are ascribed to the near band edge (NBE) and deep level electron transitions. The PL emissions of the metal-semiconductor concentric solid Zn/ZnO nanospheres are attributed to the electron transitions across the metal-semiconductor junction, from the E_F to the valence and 3d bands, and from the interface states to the valence band. All three nanostructures are excellent room-temperature light emitters.

Semiconducting hollow ZnO nanoballoons and metal-semiconductor concentric solid Zn/ZnO nanospheres were synthesized from metallic solid Zn nanospheres by a unique thermal radiation method. All the various hollow and solid ZnO nanostructures are well known to possess optical and PL properties[1–5]. Recently, we found that metallic Zn nanoplates also have unique PL emissions[6], but the PL emission mechanism is different from that of semiconducting ZnO nanostructures. These promising PL characteristics give these materials the potential for applications in optical amplification and lasing. It is difficult to distinguish between the chemical, structural and PL properties of Zn and ZnO, because they are so similar to each other[6]. Here we show the varying PL emission mechanisms for metallic solid Zn nanospheres, semiconducting hollow ZnO nanoballoons, and metal-semiconductor concentric solid Zn/ZnO nanospheres. The PL emissions of the metallic solid Zn nanospheres are mainly dependent on the electron transitions between the Fermi level (E_F) and the 3d band[6], while those of the semiconducting hollow ZnO nanoballoons are ascribed to the near band edge (NBE)[1,2,7] and deep level[8,9] electron transitions. The PL emissions of the metal-semiconductor concentric solid Zn/ZnO nanospheres are attributed to the electron transitions across the metal-semiconductor junction, from the E_F to the valence and 3d bands, and from the interface states to the valence band. All three nanostructures have good and effective visible-light emissions at room temperature, so they all are potential candidates for use in optoelectronic nano-devices, such as light-emitting diodes (LEDs) and laser diodes (LDs).

Over the past two decades, research on nanostructures has become more and more popular in various scientific fields, because nanostructures possess fascinating and fanciful properties that make them useful in many practical applications[10,11]. Compared to solid micro- and nano-structures, hollow micro- and nano-structures obviously have much lower density and larger surface-to-volume ratios. Among the metal oxides, zinc oxides (ZnO) are most likely to form varying hollow micro- and nano-structures[1,2,7,12–24], and to be the most functional materials

finding many applications including in biosensors[25], solar cells[26], photocatalysis[4,27], light emitting diodes[3,5], gas sensing[28], field-emission[29,30], and generators[31–34]. Many growth methods have been used to prepare various hollow ZnO micro- and nano-structures[3,7,12,13,16,17,19,22–26,35–37], but the template methods are generally the most popular and common techniques[7,12,13,16,17,19,22–26,35–37]. Chemical solutions containing Zn and O ions are usually used in the template methods, and both ions are assembled on the templates so as to construct hollow ZnO micro- and nano-structures. Another growth method used for synthesizing hollow ZnO micro- and nano-structures is the oxidation technique[7,23,24]. Zn micro- and nano-particles can also be oxidized to become hollow ZnO micro- and nano-structures by annealing at the low temperature of ∼440°C[23]. In fact, the Zn nanoparticles cannot be oxidized until the annealing temperature reaches ∼100°C[38] because of the filled 3d and 4s orbital bands of Zn, which also makes it a good anti-corrosion agent[39].

Surface morphology. Fig. 1 shows the surface morphology and chemical characteristics of solid nanospheres and hollow nanoballoons. Examination of the FESEM and TEM images in Fig. 1a and 1b shows considerable quantities of solid nanospheres and hollow nanoballoons randomly distributed on Si substrates. From Fig. 1a, it can be seen that the solid nanospheres are ∼100–500 nm in diameter before annealing. The high-magnification TEM image in the inset to Fig. 1a shows a single solid nanosphere of ∼190 nm wide. Fig. 1b shows hollow nanoballoons about ∼150–600 nm in diameter that formed after the annealing of the solid nanospheres at 400°C. The high-magnification TEM image in the inset to Fig. 1b shows a single hollow nanoballoon of ∼300 nm wide, with a wall that is ∼18 nm thick. The wall of the hollow nanoballoon looks very patchy, because it is comprised of small grains. In the experiments, the solid nanospheres were not only annealed at 400°C, but also 100, 200, 300°C, respectively. The surface morphology of various solid nanospheres before and after annealing at 100, 200, 300, and 400°C can be seen in the FESEM and TEM images in Fig. S1 (Supplemental Information). The solid nanospheres appeared unchanged at annealing temperatures of 100, 200, and 300°C, but hollow nanoballoons formed at an annealing temperature of 400°C. The results indicate that the solid nanospheres were only entirely transformed into hollow nanoballoons by the thermal radiation method when the annealing temperature was higher than 300°C.

Chemical characteristics. EDS can be exploited for qualitative analysis of the chemical composition on the surfaces of the solid nanospheres and hollow nanoballoons. The EDS spectra for the solid nanospheres and hollow nanoballoons are shown in Fig. 1c. In the lower panel of Fig. 1c, one can only see EDS peaks for the elements Zn and Si for the nanospheres before annealing. Obviously, the Si signals originate from the Si substrate. The results imply that prior to annealing, the nanospheres are pure Zn; no ZnO is included at all. This EDS results are in agreement with those obtained in a
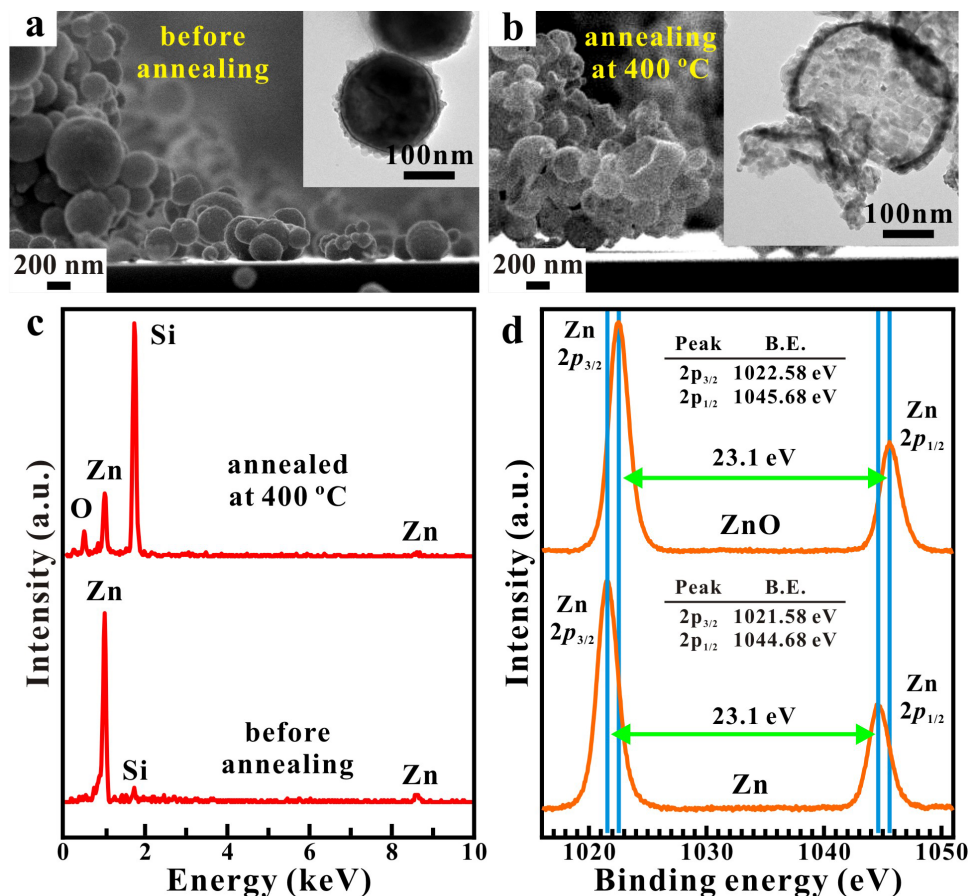

Figure 1 | Surface morphology and chemical characteristics. (a), A field-emission scanning electron microscopy (FESEM) image of solid nanospheres of ∼100-500 nm wide. A transmission electron microscopy (TEM) image (inset) of a single solid nanosphere of ∼190 nm wide. (b), An FESEM image of hollow nanoballoons of ∼150-600 nm wide. The hollow nanoballoons formed after the nanospheres were annealed at 400°C. A TEM image (inset) of a single nanoballoon of ∼300 nm wide. The wall of the single nanoballoon was made up of many small grains of ∼18 nm thick. (c), Two energy dispersive spectroscopy (EDS) spectra for solid nanospheres before and after annealing at 400°C and hollow nanoballoons. (d), Two X-ray photoelectron spectroscopy (XPS) spectra for Zn and ZnO.

previous study[38]. The EDS spectra for nanoballoons that appear in the upper panel of Fig. 1c show an oxygen (O) peak along with those for Zn and Si, suggesting the presence of ZnO after annealing at 400°C. A series of EDS spectra were also obtained after annealing at temperatures of 100, 200, and 300°C (see Fig. S2, Supplemental Information). Surprisingly, the EDS results show no oxidation at all of the solid Zn nanospheres when the annealing temperature was 200°C, but they were clearly oxidized when the annealing temperature rose above 300°C. This is why Zn is a good anti-oxidation material at temperatures below 200°C. However, the EDS signals may indicate the condition inside of the solid nanospheres, not whether the surfaces have been oxidized or not. XPS is a powerful analytical technique for examining the surface oxidation of solid nanospheres, because the signals come from the surfaces of ~10 nm thick. Hence, it is preferable to use XPS which is very surface sensitive and capable of quantitative evaluation of the electronic structures and chemical characteristics of the specimens. Fig. 1d illustrates the XPS spectra for Zn (lower panel) and ZnO (upper panel). Note that the binding energies of Zn $2p_{3/2}$ and $2p_{1/2}$ of Zn and ZnO are very close, and the chemical shifts between Zn $2p_{3/2}$ and $2p_{1/2}$ are the same for Zn and ZnO. The similarity in the XPS spectra makes it difficult to distinguish between the Zn and ZnO, but the small differences in the binding energy help us determine the difference between Zn and ZnO. In fact, a series of

XPS spectra were obtained before and after annealing at temperatures of 100, 200, 300, and 400°C (see Fig. S3, Supplemental Information). The XPS spectrum in the lower panel of Fig. 1d represents the chemical characteristics of the Zn solid nanospheres before annealing and after annealing at 100 and 200°C; the spectra in the upper panel of Fig. 1d are those of the solid Zn nanospheres after annealing at 300 and 400°C. The XPS results confirm that there was no oxidation of the solid Zn nanospheres at an annealing temperature of 200°C, but there was clear oxidation when the annealing temperature exceeded 300°C.

Crystalline structure determination. XRD is a good technique for revealing details of the crystalline structures and crystal growth formation during synthesis. Fig. 2a shows the three XRD spectra for the solid Zn nanospheres before annealing and after annealing at 100 and 200°C (lower panel), and for the solid Zn nanospheres after annealing at 300°C (middle panel), and after annealing at 400°C (upper panel). The three XRD spectra in Fig. 2a are clearly different from one another. In the lower panel, the diffraction peaks at $2\theta =$ 36.5°, 39.2°, and 43.4° correspond respectively to the (002), (100), and (101) lattice planes of the hexagonal Zn crystal in the space group $P6_3/mmc$, with lattice constants of $a = b = 0.2659$ nm, $c = 0.4935$ nm, $\alpha = \beta = 90°$, $\gamma = 120°$ (JCPDS 01-1238). In the middle panel, the diffraction peaks appear not only at $2\theta = 36.5°$, 39.2°, and
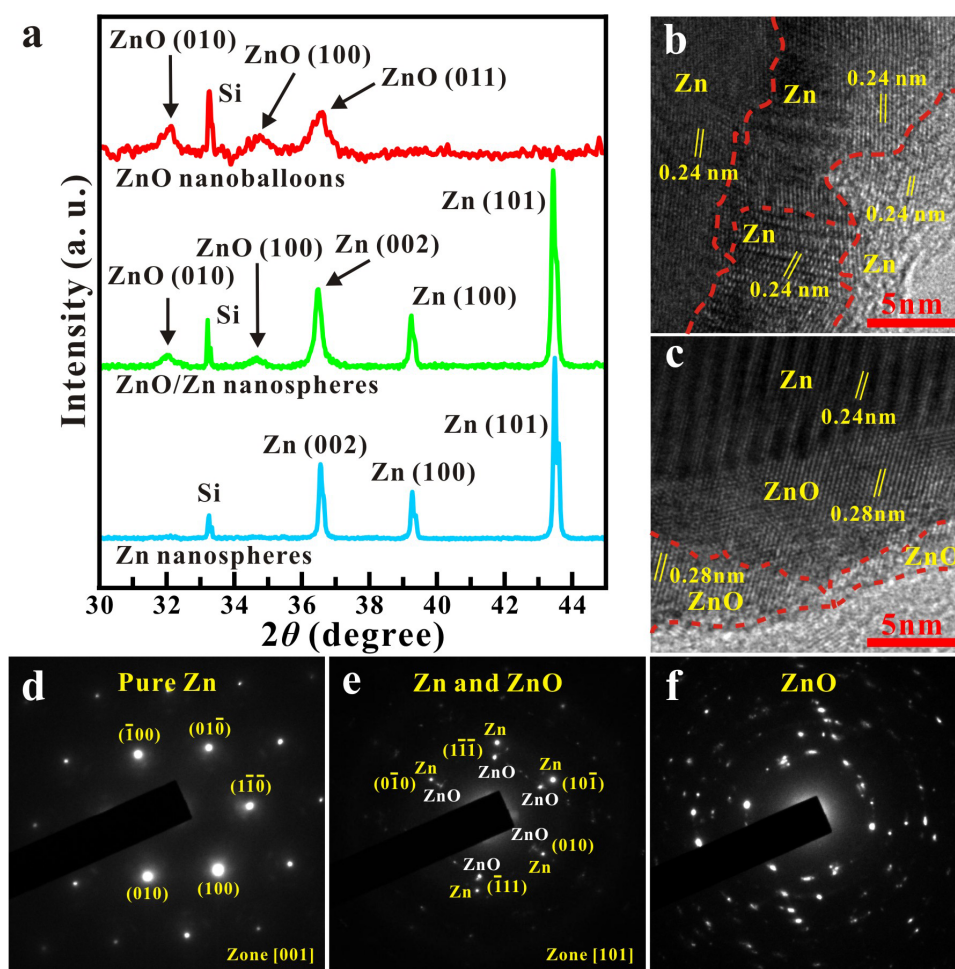
Figure 2 | Crystalline structure determination. (a), Three X-ray diffractometry (XRD) spectra for the solid Zn nanospheres before annealing and after annealing at 100 and 200°C (lower panel), after annealing at 300°C (middle panel), and after annealing at 400°C (upper panel). (b), A high-magnification TEM image of the solid Zn nanospheres. (c), A high-magnification TEM image of the concentric solid Zn/Zn nanospheres. (d), A selected-area electron diffraction (SAED) pattern of the solid Zn nanospheres. (e), An SAED pattern of the concentric solid Zn/Zn nanospheres. (f), An SAED pattern of the hollow ZnO nanoballoons.

3
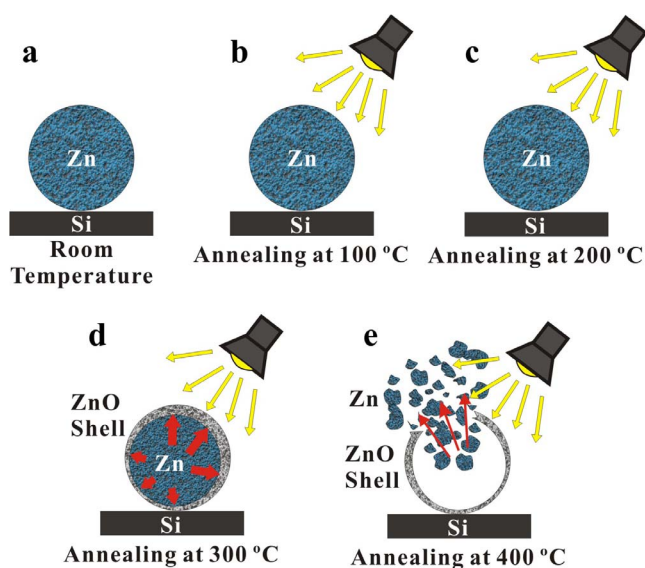
Figure 3 | Growth mechanisms. (a-e), Schematic diagrams showing growth mechanisms for the concentric solid Zn/ZnO nanospheres and hollow ZnO nanoballoons. The solid Zn nanospheres showed no oxidization at 200°C. The concentric solid Zn/ZnO nanospheres and hollow ZnO nanoballoons formed at 300 and 400°C, respectively.

43.4°, but also at $2\theta = 32.0°$ and 34.7°. Obviously, the three diffraction peaks at $2\theta = 36.5°$, 39.2°, and 43.4° embody pure Zn crystal, while the small diffraction peaks at $2\theta = 32.0°$ and 34.7° correlate to the (010) and (100) lattice planes of the hexagonal ZnO crystal in the space group $P6_3/mmc$ with lattice constants of $a = b = 0.3242$ nm, $c = 0.5188$ nm, $\alpha = \beta = 90°$, $\gamma = 120°$ (JCPDS 36-1451). In the upper panel, the diffraction peaks at $2\theta = 32.0°$, 34.7°, and 36.6° symbolize only the ZnO crystal. The diffraction peak at 36.6° corresponds to the (011) lattice plane of the hexagonal ZnO crystal, although it is very close to that at 36.5° for the (002) lattice plane of the hexagonal Zn crystal. Note that all the diffraction peaks at 33.2° represent the Si substrates. A series of XRD spectra was obtained at room temperature and at annealing temperatures of 100, 200, 300, and 400°C, respectively (see Fig. S4, Supplemental Information). As with the EDS data, the XRD results also agree that there was not oxidation of the solid Zn nanospheres at an annealing temperature of 200°C, but there was clear oxidization when the annealing temperature exceeded 300°C. Only the surfaces of the solid Zn nanospheres were oxidized after annealing at 300°C, the inner cores were still pure Zn metal. Therefore, concentric solid Zn/ZnO nanospheres formed at an annealing temperature of 300°C. The Zn solid nanospheres were completely transformed into hollow ZnO nanoballoons at an annealing temperature of 400°C.

The high-magnification TEM images in Figs. 2b and 2c show two edge portions of the solid Zn nanospheres before and after annealing at 300°C in atomic resolution. The two edge portions are taken from the edge regions in the areas highlighted by the red rectangular boxes in Figs. S1a and S1d. In Fig. 2b, one can clearly see the surface and core fractions of the solid Zn nanosphere. The core fractions are pure Zn crystals, and the lattice constants between two adjacent parallel atomic lattice-fringes are 0.24 nm. The surface fractions of the solid Zn nanosphere are comprised of many grains, with the surface grains also being pure Zn crystals, as indicated by the lattice constant of 0.24 nm. The results are in good agreement with those obtained in previous studies[40]. The SAED pattern in Fig. 2d, taken from the selected area in Fig. S1a, shows a set of six-fold symmetrical diffraction spots indexed to the [100] zone axis. The reflections in the SAED pattern indicated that the solid Zn nanospheres are hexagonal single

crystals of Zn. The core and surface of the concentric solid Zn/ZnO nanospheres are also clearly observable in Fig. 2c. The core is pure Zn crystal with a lattice constant of 0.24 nm, but the surface is not. The surface of the concentric solid Zn/ZnO nanospheres consists of many grains. The surface grains are ZnO crystals, with lattice constants of 0.28 nm, in agreement with previous studies[40]. The SAED pattern in Fig. 2e, taken from the selected area in Fig. S1d, shows two obvious sets of six-fold symmetric and concentric diffraction spots indexed to the [101] zone axis. The two sets of reflections are also indicative of Zn and ZnO, verifying that after annealing at 300°C, the solid Zn nanospheres become concentric solid Zn/ZnO nanospheres. However, the SAED pattern in Fig. 2f, taken from the selected area (in the red rectangular box in Fig. S1e) shows disordered diffraction spots, suggesting that the hollow ZnO nanoballoons are comprised of polycrystalline and fine grains of ZnO. Based on the EDS, XPS, XRD and TEM results, we can present a growth mechanism for the transformation of solid Zn nanospheres to concentric solid Zn/ZnO nanospheres and hollow ZnO nanoballoons.

Growth mechanism. Fig. 3 shows a schematic diagram of the growth mechanisms for the concentric solid Zn/ZnO nanospheres and hollow ZnO nanoballoons. As shown in Figs. 3a–3c, there is no oxidation of the Zn solid nanospheres when the annealing temperature is 200°C or less. The thermal radiation annealing is carried out using a halogen lamp. At an annealing temperature of 300°C, the surfaces of the solid Zn nanospheres become oxidized and are transformed into ZnO nanoshells, but the inner nanocores remain pure metallic Zn. The concentric solid Zn/ZnO nanospheres are formed as illustrated in Fig. 3d. Due to thermal heating, the inner Zn nanocores of the concentric Zn/ZnO nanospheres expand against the ZnO nanoshells during annealing. However, the ZnO nanoshells confine the expansion, creating high internal pressure in the inner Zn nanocores. The red arrows represent the internal pressure against the ZnO nanoshells from the expansion of the inner Zn nanocores. The pressure is higher for an annealing temperature of 400°C than at 300°C. As seen in Fig. 1b, the nanoshells of the hollow nanoballoons are patched by many small grains during thermal radiation annealing, so cracks are unsurprisingly present among the small grains. When the internal pressures reach a critical point during annealing at about 400°C, the concentric Zn/ZnO nanospheres burst, as shown in Fig. 3e. The inner Zn nanocores are split into many nanoparticles that explode out leaving only hollow ZnO nanoballoons with nanoshells ~18 nm.

Photoluminescence emission mechanisms. PL spectroscopy is a good optical method for probing the electron transitions between the high and low energy states, allowing investigation of the impurities, defects, and bandgaps in semiconductor materials. This method shows not only energy states, but also the electron densities of states for electron transitions, which supply more electronic information. Fig. 4 shows the room-temperature PL spectra (a–c) and PL emission mechanisms (d–f), for the metallic Zn solid nanospheres, semiconducting hollow ZnO nanoballoons, and metal-semiconductor concentric solid Zn/ZnO nanospheres, respectively. Fig. 4a displays the PL spectrum of the metallic solid Zn nanospheres, which is comprised of a high-intensity emission band centered at 408 nm and a low-intensity broad emission band from ~450 to 700 nm. The schematic diagram appearing in the inset to Fig. 4a illustrates the high-intensity purple light emitted from a metallic solid Zn nanosphere. The high-intensity emission band at 408 nm corresponds to an energy of ~3.04 eV. According to a previous study[6], the high-intensity band at 408 nm is critically dependent on the interband electron transitions among the $3d$ band, sp-conduction band, and Fermi level (E_F) of the metallic solid Zn nanospheres. The schematic diagram in Fig. 4d shows the electron transitions (or PL emissions) between the E_F and $3d$ band for the metallic solid Zn nanospheres. The incident 266-nm laser
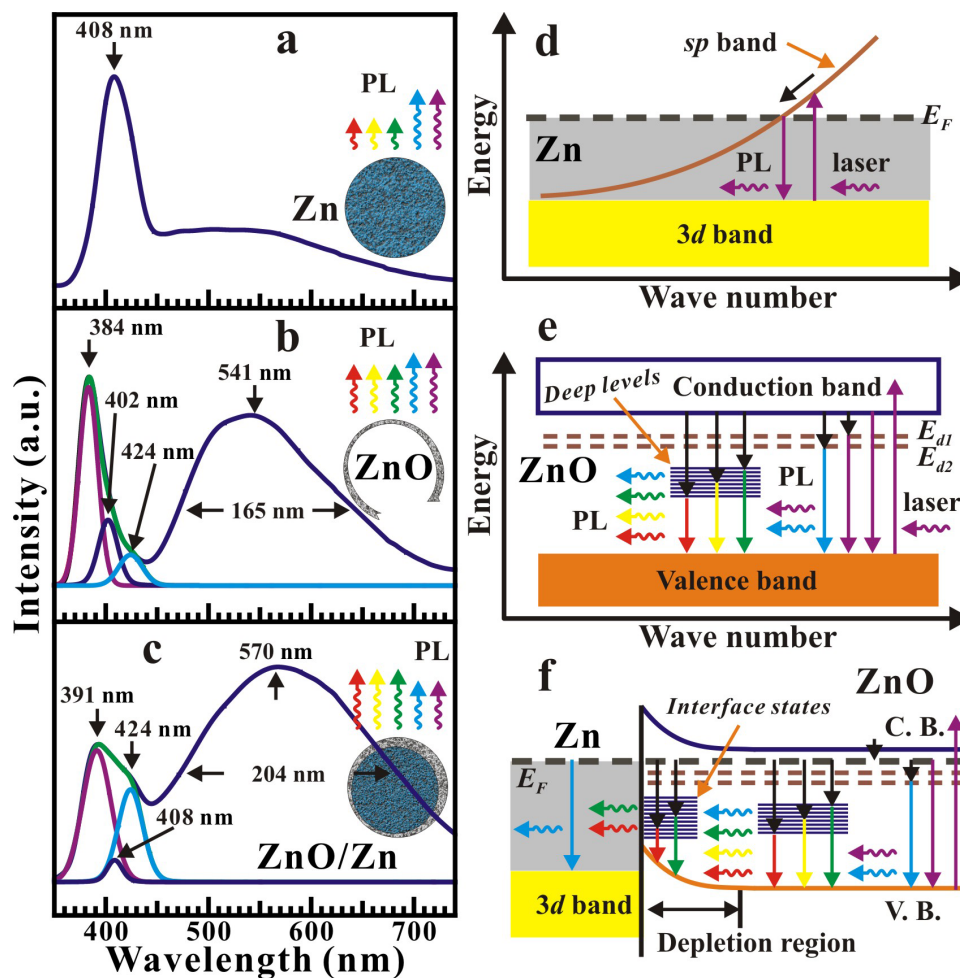
Figure 4 | Room-temperature photoluminescence (PL) emission mechanisms. (a-c), PL spectra for the solid Zn nanospheres, hollow ZnO nanoballoons, and concentric solid Zn/ZnO nanospheres. (d-f), Schematic diagrams of the band structures for the three various PL emission mechanisms for the metallic solid Zn nanospheres, semiconducting hollow ZnO nanoballoons, and metal-semiconductor concentric solid Zn/ZnO nanospheres.

(indicated by an upward pointing purple arrow) excites electrons lying in the 3d band to move to unoccupied states in the sp-conduction band above the E_F. The excited electrons then descend to the E_F in nonradiative electron transitions (indicated by a black arrow). The electrons at the E_F have to drop back so as to recombine with the holes in the 3d band, releasing energy through radiation of the purple light emission (indicated by a downward pointing purple arrow). In addition, the two-dimensional (2D) pure Zn-metal nanoplates also possess semiconducting characteristics[6], so the metallic solid Zn nanospheres have similar semiconducting properties. The low-intensity broad emission band occurs due to the electron transitions from the conduction band to the valence band for visible light emissions from green to red.

The PL spectrum for the semiconducting hollow ZnO nanoballoons shown in Fig. 4b includes a sharp ultraviolet (UV) emission band and a broad visible emission band centered at 384 and 541 nm corresponding to the energies of ~3.23 and ~2.29 eV, respectively. The inset to Fig. 4b shows a schematic diagram of the UV and visible light emitted from a semiconducting hollow ZnO nanoballoon. The sharp UV light emission band at 384 nm is attributed to the near band edge (NBE) electron transition[1,2,7] between the conduction band and the valence band, and indicates that the bandgap for the hollow ZnO nanoballoons is 3.23 eV. In fact, the sharp UV light emission band can be decomposed into three emission peaks centered at 384, 402, and 424 nm. The large peak at 384 nm of course represents the NBE electron transition, while the two small peaks at

402 and 424 nm symbolize the two donor states (E_{d1} and E_{d2}). The E_{d1} and E_{d2} indicate that the hollow ZnO nanoballoons are n-type semiconductors, and the electron transitions from the E_{d1} and E_{d2} to the valence band release blue light emissions with energies of 3.08 and 2.92 eV, respectively. The broad visible light emission band is ascribed to the electron transitions between the deep levels and the valence band[8,9]. The deep levels are created by structural defects, impurities, Zn residues, and oxygen vacancies[1,2,7] within the band-gap, but mainly from the various oxygen vacancies[7,41,42]. The electron transitions (or PL emissions) from the conduction band, donor states (indicated by brown dashed lines), and deep levels (indicated by deep blue lines) to the valence band for the semiconducting hollow ZnO nanoballoons are schematically illustrated in Fig. 4e. The incident 266-nm laser (indicated by an upward pointing purple arrow) excites electrons lying in the valence band to move to the conduction band. Some excited electrons drop directly back to the valence band, and the UV light (indicated by a downward pointing purple arrow) is then emitted. However, the large excited electrons first undergo non-radiative electron transitions (indicated by black arrows) to the donor states and the various deep levels, and then return to the valence band to radiate varying visible light emissions (indicated by purple, blue, green, yellow, and red arrows) from purple to red.

The PL spectrum of the metal-semiconductor concentric solid Zn/ZnO nanospheres, which contains a UV-blue emission band and broad visible emission bands centered at 391 and 570 nm, corresponding to the energies of ~3.17 and ~2.17 eV, respectively, is
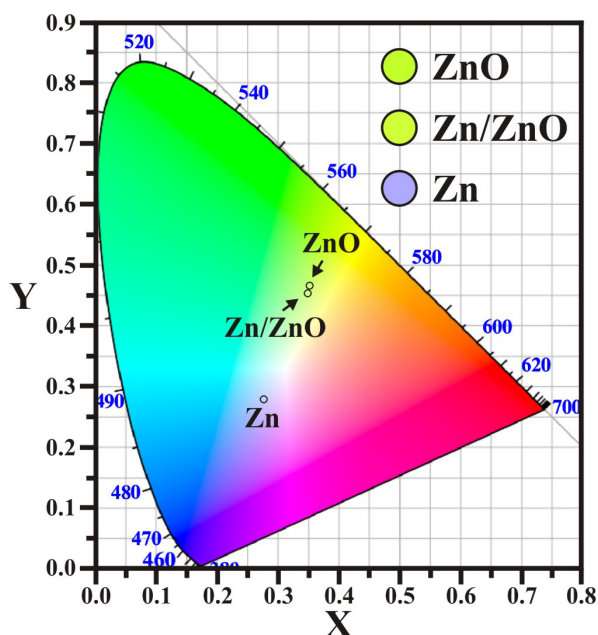
Figure 5 | Color space chromaticity diagram. Color space chromaticity diagram showing the colors of the PL emissions from the semiconducting hollow ZnO nanoballoons, metal-semiconductor concentric solid Zn/ZnO nanospheres, and metallic solid Zn nanospheres. Both the hollow ZnO nanoballoons and concentric solid Zn/ZnO nanospheres look light-green. The metallic solid Zn nanospheres appear light-purple.

illustrated in Fig. 4c. The inset to Fig. 4c shows a schematic diagram of the UV-blue and visible light emitted from a metal-semiconductor concentric solid Zn/ZnO nanosphere, comprised of an inner metallic Zn nanocore and a ZnO nanoshell. The UV-blue emission band can be decomposed into three emission peaks centered at 391, 408, and 424 nm. The two large peaks at 391 and 424 nm originate from the semiconducting ZnO nanoshells, while the small peak at 408 nm comes from the inner metallic Zn nanocores. Obviously, the peak at 424 nm also embodies the electron transition from the E_{d2} to the valence band of the semiconducting ZnO nanoshells, indicating that the ZnO nanoshells are also n-type semiconductors. The peak at 408 nm represents the electron transition from the E_F to the $3d$ band of the inner metallic Zn nanocores. The ZnO nanoshells can block and absorb the light emissions from the inner metallic Zn nanocores, so the intensity of the blue light at 408 nm is much reduced when compared with that shown in Fig. 4a. The peak at 391 nm is definitely different from that at 384 nm, so it is not originated from the NBE electron transition. The redshift from 384 to 391 nm for the NBE electron transition is also not considered to be due to the quantum confinement effect. The ZnO nanoballoons and nanoshells are close to each other in size, so there are other reasons for the redshift. In addition, the visible emission band centered at 570 nm is much broader than that centered at 541, as shown in Fig. 4b, and its intensity is also higher than that of the UV-blue emission band. Therefore, the other PL emission mechanisms are suggested for the metal-semiconductor concentric solid Zn/ZnO nanospheres.

The schematic diagram in Fig. 4f shows the electron transitions (or PL emissions) in the metal-semiconductor junction for the inner Zn nanocores in contact with the ZnO nanoshells, namely the metal-semiconductor concentric solid Zn/ZnO nanospheres. It is known that when metallic Zn comes into contact with n-type ZnO, Schottky contacts form at the interface of the metal-semiconductor junction due to the Fermi level pinning effect[8,43]. Therefore, the E_F of the metallic Zn nanocores is pinned just below and very close to the conduction bands of the n-type ZnO nanoshells[8,43]. The peak at 391 nm indicates the E_F to be 0.06 eV below the conduction bands

of the n-type ZnO nanoshells. When the incident 266-nm laser (indicated by an upward pointing purple arrow) excites electrons from the valence band to the conduction band, the electrons lying in the E_F immediately recombine with the holes in the valence band to emit UV light (indicated by a downward pointing purple arrow). The intensity of the peak of 391 nm is visibly higher than that of the peak of 424 nm, implying that the density of electrons in the E_F is larger than that in the E_{d2}, because the inner Zn nanocores can inject plenty of free electrons into the ZnO nanoshells at the E_F. The peak at 424 nm, corresponding to a blue light emission (indicated by a blue arrow), is indicative of the electron transition between the E_{d2} and the valence band. The density of electrons in the E_{d1} is much less, as indicated by the barely observable corresponding PL emission peak in Fig. 4c. However, the intensity of the broad visible emission band centered at 570 nm is apparently larger than that of the UV-blue emission band centered at 391 nm. It is known that when a metal comes into contact with a semiconductor, electron states like deep levels are induced at the interface between the metal and the semiconductor. For the metal-semiconductor concentric solid Zn/ZnO nanospheres, many interface states are naturally produced at the interfaces. The density of electrons given by the deep level and interface states create a much larger PL intensity than those brought from the E_F or E_{d2}. Therefore, large excited electrons undergo nonradiative electron transitions (indicated by black arrows) to the various deep levels and interface states, then return to the valence band to radiate more varying visible light emissions (indicated by purple, blue, green, yellow, and red arrows) from purple to red. This is the reason why the intensity of the broad visible emission band centered at 570 nm is much higher than that of the UV-blue emission band centered at 391 nm.

Color space chromaticity diagram. The colors of the PL emissions from the semiconducting hollow ZnO nanoballoons, metal-semiconductor concentric solid Zn/ZnO nanospheres, and metallic solid Zn nanospheres are shown in the color space chromaticity diagram in Fig. 5. Obviously, both the semiconducting hollow ZnO nanoballoons and metal-semiconductor concentric solid Zn/ZnO nanospheres appear a very similar light-green, although the intensities and band positions of the two PL spectra are different. According to the PL spectra in Fig. 4, the light-green colors consist of varying visible light emissions from purple to red. However, the metallic Zn solid nanospheres appear light-purple, indicating the color to be mainly comprised of purple and blue light emissions. Three circular monoliths consisting of solid Zn nanospheres, solid Zn/ZnO nanospheres, and hollow ZnO nanoballoons, respectively, are made, and each circular monolith is 5 mm in diameter. (see Fig. S5, Supplemental Information) All the three circular monoliths have effective visible-light emissions at room temperature, so all the three nanostructures are potential candidates for use in optoelectronic nanodevices, such as light-emitting diodes and laser diodes in purple and green.

Summary. Semiconducting hollow ZnO nanoballoons and metal-semiconductor concentric solid Zn/ZnO nanospheres were synthesized from metallic solid Zn nanospheres using a unique thermal radiation method. All of the various hollow and solid ZnO nanostructures are well known to possess optical and photoluminescent properties. Recently, it has also been found that metallic Zn nanoplates have unique photoluminescent emissions, but the PL emission mechanism is different from that of semiconducting ZnO nanostructures. These promising PL characteristics give them potential applications in optical amplification and lasing. Here we show three distinctive PL emission mechanisms for metallic solid Zn nanospheres, semiconducting hollow ZnO nanoballoons, and metal-semiconductor concentric solid Zn/ZnO nanospheres. All three nanostructures have good and effective visible-light emissions at room temperature, so they are all potential candidates for use in

optoelectronic nanodevices, such as light-emitting diodes and laser diodes.

Methods

Semiconducting hollow ZnO nanoballoons and metal-semiconductor concentric solid Zn/ZnO nanospheres were synthesized using the thermal radiation method. Samples of metallic Zn powder (99% pure purchased from Aldrich) were immersed in alcohol solutions. Then 10 ml pipettes were used to pick up samples from the top of the alcohol solution to extract metallic solid Zn nanospheres. A few drops of alcohol solution were placed on a Si substrate. After drying, only the metallic solid Zn nanospheres remained on the Si substrate. A halogen lamp was used to anneal the metallic solid Zn nanospheres at a pressure of 1×10^{-6} Torr at 100, 200, 300, and 400°C, for 10 minutes. The surfaces of the metallic Zn solid nanospheres were oxidized to form ZnO layers when the annealing temperature was above 200°C, so metal-semiconductor concentric solid Zn/ZnO nanospheres and semiconducting hollow ZnO nanoballoons were thus produced at 300 and 400°C, respectively. The surface morphology of the solid Zn nanospheres, concentric solid Zn/ZnO nanospheres, and hollow ZnO nanoballoons was examined by an FESEM (JOEL JSM-6500F) equipped with an EDS (Oxford instrument INCA, X-sight 7557). The crystalline structures of the solid Zn nanospheres, concentric solid Zn/ZnO nanospheres, and hollow ZnO nanoballoons were examined by an XRD (X'Pert Pro) with Cu Kα radiation (λ= 1.541 Å) and a TEM (JOEL JEM-2100) with an SAED. The elemental information about the solid Zn nanospheres, concentric solid Zn/ZnO nanospheres, and hollow ZnO nanoballoons was quantitatively analyzed based upon XPS (Thermo Scientific, K-Alpha) with an Al Kα beam of 1486.6 eV. The PL properties of the metallic solid Zn nanospheres, metal-semiconductor concentric solid Zn/ZnO nanospheres, and semiconducting hollow ZnO nanoballoons were studied by a spectral imaging spectrometer (Triax 320) with a Q-switched diode-pumped solid state 266 nm laser operated at 1 kHz acting as the pumping light source.

1. Khan, A., Jadwisienczak, W. M. & Kordesch, M. E. From Zn microspheres to hollow ZnO microspheres: A simple route to the growth of large scale metallic Zn microspheres and hollow ZnO microspheres. *Phys. E* **33**, 331–335 (2006).
2. Umar, A., Kim, S. H., Im, Y. H. & Hahn, Y. B. Structural and optical properties of ZnO micro-spheres and cages by oxidation of metallic Zn powder. *Superlattices Microstruct.* **39**, 238–246 (2006).
3. Zimmler, M. A., Voss, T., Ronning, C. & Capasso, F. Exciton-related electroluminescence from ZnO nanowire light-emitting diodes. *Appl. Phys. Lett.* **94**, 241120 (2009).
4. Chu, D., Masuda, Y., Ohji, T. & Kato, K. Formation and photocatalytic application of ZnO nanotubes using aqueous solution. *Langmuir* **26**, 2811–2815 (2010).
5. Lupan, O., Pauporte, T., Le Bahers, T., Viana, B. & Ciofini, I. Wavelength-emission tuning of ZnO nanowire-based light-emitting diodes by Cu doping: experimental and computational insights. *Adv. Funct. Mater.* **21**, 3564–3572 (2011).
6. Lin, J.-H. *et al.* Room-temperature wide-range photoluminescence and semiconducting characteristics of two-dimensional pure metallic Zn nanoplates. *RSC Adv.* **2**, 2123–2127 (2012).
7. Sulieman, K. M., Huang, X., Liu, J. & Tang, M. Controllable synthesis and characterization of hollow-opened ZnO/Zn and solid Zn/ZnO single crystal microspheres. *Nanotechnology* **17**, 4950–4955 (2006).
8. Bylander, E. G. Surface effects on the low-energy cathodoluminescence of zinc oxide. *J. Appl. Phys.* **49**, 1188–1195 (1978).
9. Srikant, V. & Clarke, D. R. On the optical band gap of zinc oxide. *J. Appl. Phys.* **83**, 5447–5451 (1998).
10. Smith, A. M. & Nie, S. Semiconductor nanocrystals: Structure, properties, and bang gap engineering. *Acc. Chem. Res.* **43**, 190–200 (2010).
11. Devan, R. S., Patil, R. A., Lin, J.-H. & Ma, Y.-R. One-dimensional metal-oxide nanostructures: Recent developments in synthesis, characterization, and applications. *Adv. Func. Mater.* **22**, 3326–3370 (2012).
12. Deng, Z., Chen, M., Gu, G. & Wu, L. A facile method to fabricate ZnO hollow spheres and their photocatalytic property. *J. Phys. Chem. B* **112**, 16–22 (2008).
13. Wu, Q. *et al.* Amino acid-assisted synthesis of ZnO hierarchical architectures and their novel photocatalytic activities. *Cryst. Growth Des.* **8**, 3010–3018 (2008).
14. Yu, J. & Yu, X. Hydrothermal synthesis and photocatalytic activity of zinc oxide hollow spheres. *Environ. Sci. Technol.* **42**, 4902–4907 (2008).
15. Zhang, L., Yan, J., Zhou, M., Yang, Y. & Liu, Y.-N. Fabrication and photocatalytic properties of spheres-in-spheres ZnO/ZnAl$_2$O$_4$ composite hollow microspheres. *Appl. Surf. Sci.* **268**, 237–245 (2013).
16. He, C.-X. *et al.* Sonochemical preparation of hierarchical ZnO hollow spheres for efficient dye-sensitized solar cells. *Chem. Eur. J.*, **16**, 8757–8761 (2010).
17. Dong, Z. *et al.* Accurate control of multishelled ZnO hollow microspheres for dye-sensitized solar cells with high efficiency. *Adv. Mater.* **24**, 1046–1049 (2012).
18. Zhang, J. *et al.* ZnO hollow spheres: Preparation, characterization, and gas sensing properties. *Sens. Actuators B-Chem.* **139**, 411–417 (2009).
19. Liu, B. & Zeng, H. C. Hollow ZnO microspheres with complex nanobuilding units. *Chem. Mater.* **19**, 5824–5826 (2007).
20. Yang, Q. & Hu, W. A novel mercury-media route to synthesize ZnO hollow microspheres. *Ceram. Int.* **36**, 989–993 (2010).
21. Liu, C., Xu, J. & Wu, Z. Direct electron transfer and electrochemical study of hemoglobin immobilized in ZnO hollow spheres. *Bioprocess. Biosyst. Eng.* **34**, 931–938 (2011).
22. Tripathy, N., Ahmad, R., Jeong, H.-S. & Hahn, Y.-B. Time-dependent control of hole-opening degree of porous ZnO hollow microspheres. *Inorg. Chem.* **51**, 1104–1110 (2012).
23. Mahapatra, A. K., Bhatta, U. M. & Som, T. Oxidation mechanism in metal nanoclusters: Zn nanoclusters to ZnO hollow nanoclusters. *J. Phys. D: Appl. Phys.* **45**, 415303 (2012).
24. Fan, H. J., Scholz, R., Kolb, F. M., Zacharias, M. & Gösele, U. Growth mechanism and characterization of zinc oxide microcages. *Solid State Commun.* **130**, 517–521 (2004).
25. Kong, T. *et al.* An amperometric glucose biosensor based on the immobilization of glucose oxidase on the ZnO nanotubes. *Sens. Actuator B-Chem.* **138**, 344–350 (2009).
26. Umar, A. Growth of comb-like ZnO nanostructures for dye-sensitized solar cells applications. *Nanoscale Res. Lett.* **4**, 1004–1008 (2009).
27. Hsu, C. C. & Wu, N. L. Synthesis and photocatalytic activity of ZnO/ZnO$_2$ cornposite. *J. Photochem. Photobiol. A-Chem.* **172**, 269–274 (2005).
28. Rout, C. S., Krishna, S. H., Vivekchand, S. R. C., Govindaraj, A. & Rao, C. N. R. Hydrogen and ethanol sensors based on ZnO nanorods, nanowires and nanotubes. *Chem. Phys. Lett.* **418**, 586–590 (2006).
29. Wang, W. *et al.* Aligned ultralong ZnO nanobelts and their enhanced field emission. *Adv. Mater.* **18**, 3275–3278 (2006).
30. Zeng, H. *et al.* Template deformation-tailored ZnO nanorod/nanowire arrays: Full growth control and optimization of field-emission. *Adv. Funct. Mater.* **19**, 3165–3172 (2009).
31. Xu, S. *et al.* Self-powered nanowire devices. *Nat. Nanotechnol.* **5**, 366–373 (2010).
32. Zhu, G. A., Yang, R. S., Wang, S. H. & Wang, Z. L. Flexible high-output nanogenerator based on lateral ZnO nanowire array. *Nano Lett.* **10**, 3151–3155 (2010).
33. Hu, Y. F., Lin, L., Zhang, Y. & Wang, Z. L. Replacing a battery by a nanogenerator with 20 V output. *Adv. Mater.* **24**, 110–114 (2012).
34. Chen, C. Y. *et al.* Anisotropic outputs of a nanogenerator from oblique-aligned ZnO nanowire arrays. *ACS Nano* **5**, 6707–6713 (2011).
35. Lou, X. W., Archer, L. A. & Yang, Z. Hollow Micro-/Nanostructures: Synthesis and Applications. *Adv. Mater.* **20**, 3987–4019 (2008).
36. Liu, J. & Xue, D. Hollow nanostructured anode materials for Li-ion batteries. *Nanoscale Res. Lett.*, **5**, 1525–1534 (2010).
37. Park, J.-E. *et al.* Photoluminescent nanographitic/nitrogen-doped graphitic hollow shells as a potential candidate for biological applications. *J. Mater. Chem. B* **1**, 1229–1234 (2013).
38. Devan, R. S. *et al.* Two-dimensional single-crystalline Zn hexagonal nanoplates: Size-controllable synthesis and X-ray diffraction study. *Nanoscale* **3**, 4339–4345 (2011).
39. Azmat, N. S., Ralston, K. D. & Cole, I. S. Pre-treatment of Zn surfaces for droplet corrosion studies. *Surf. Coat. Technol.* **205**, 928–935 (2010).
40. Hu, J. Q., Li, Q., Meng, X. M., Lee, C. S. & Lee, S. T. Thermal reduction route to the fabrication of coaxial Zn/ZnO nanocables and ZnO nanotubes. *Chem. Mater.* **15**, 305–308 (2003).
41. Devan, R. S. *et al.* High room-temperature photoluminescence of one-dimensional Ta$_2$O$_5$ nanorod arrays. *Nanotechnology* **20**, 445708 (2009).
42. Devan, R. S. *et al.* Enhancement of green-light photoluminescence of Ta$_2$O$_5$ nanoblock stacks. *Phys. Chem. Chem. Phys.* **13**, 13441–13446 (2011).
43. Sze, S. M. *Physics of Semiconductor Devices* (John Wiley, New York, 1981).

Acknowledgments

Author contributions

Y.-R.M. conceived and designed the study. J.-H.L. and R.A.P. contributed equally to this work. J.-H.L. and Z.-A.L. prepared and characterized the samples. R.A.P. and R.S.D. analyzed the data and produced the results. Y.-P.W. and C.-H.H. performed the PL experiments. Y.-R.M. wrote the manuscript in consultation with Y.L.

Additional information